



Direct visualization and characterization of the human zona incerta and surrounding structures

Jonathan C. Lau^{1,2,3,4} | Yiming Xiao^{2,3} | Roy A. M. Haast^{2,3} |
Greydon Gilmore^{1,4} | Kâmil Uludağ^{7,8,9} | Keith W. MacDougall¹ |
Ravi S. Menon^{2,3,6} | Andrew G. Parrent¹ | Terry M. Peters^{1,2,3,4,6} |
Ali R. Khan^{1,2,3,4,5,6}

¹Department of Clinical Neurological Sciences,
Division of Neurosurgery, Western University,
London, Ontario, Canada

²Imaging Research Laboratories, Robarts
Research Institute Canada, Western
University, London, Ontario, Canada

³Centre for Functional and Metabolic
Mapping, Robarts Research Institute, Western
University, London, Ontario, Canada

⁴School of Biomedical Engineering, Western
University, London, Ontario, Canada

⁵Brain and Mind Institute, Western University,
London, Ontario, Canada

⁶Department of Medical Biophysics, Western
University, London, Ontario, Canada

⁷IBS Center for Neuroscience Imaging
Research, Sungkyunkwan University, Suwon,
South Korea

⁸Department of Biomedical Engineering, N
Center, Sungkyunkwan University, Suwon,
South Korea

⁹Techna Institute and Koerner Scientist in MR
Imaging, University Health Network, Toronto,
Ontario, Canada

Correspondence

Jonathan C. Lau, Department of Clinical
Neurological Sciences, Division of
Neurosurgery, Western University, London,
ON, Canada.
Email: jonathan.c.lau@gmail.com

Funding information

CIHR Foundation, Grant/Award Number: FDN
201409

Abstract

The zona incerta (ZI) is a small gray matter region of the deep brain first identified in the 19th century, yet direct *in vivo* visualization and characterization has remained elusive. Noninvasive detection of the ZI and surrounding region could be critical to further our understanding of this widely connected but poorly understood deep brain region and could contribute to the development and optimization of neuromodulatory therapies. We demonstrate that high resolution (submillimetric) longitudinal (T1) relaxometry measurements at high magnetic field strength (7 T) can be used to delineate the ZI from surrounding white matter structures, specifically the fasciculus cerebellothalamicus, fields of Forel (fasciculus lenticularis, fasciculus thalamicus, and field H), and medial lemniscus. Using this approach, we successfully derived *in vivo* estimates of the size, shape, location, and tissue characteristics of substructures in the ZI region, confirming observations only previously possible through histological evaluation that this region is not just a space between structures but contains distinct morphological entities that should be considered separately. Our findings pave the way for increasingly detailed *in vivo* study and provide a structural foundation for precise functional and neuromodulatory investigation.

KEY WORDS

7 T, atlas, brain, deep brain stimulation, human, neuroanatomy, quantitative MRI, T1, zona incerta

Terry M. Peters and Ali R. Khan are joint senior authors.

This is an open access article under the terms of the Creative Commons Attribution License, which permits use, distribution and reproduction in any medium, provided the original work is properly cited.

© 2020 The Authors. *Human Brain Mapping* published by Wiley Periodicals LLC.

1 | INTRODUCTION

The zona incerta (ZI) is a small but diffuse structure in the deep brain first identified by Auguste Forel in 1877, famously described as “an immensely confusing area about which nothing can be said” (Forel, 1877). Forel appreciated that the ZI consisted of gray matter located between the external medullary lamina of the thalamus and the corpus Luysi (subthalamic nucleus; STN) of otherwise “indefinite” description. It is telling that Forel found the ZI so difficult to describe given his crucial role in the delineation of surrounding white matter tracts still referred to eponymously as the fields of Forel (Gallay, Jeanmonod, Liu, & Morel, 2008). Since its original description, much has been learned about the ZI and surrounding structures although robust *in vivo* visualization has remained elusive.

The anatomical boundaries of the ZI have generally been described in the context of its more discrete neighbors rather than based on any consistent feature of the region itself. Packed in a small area between the ventral thalamus, STN, and red nucleus (RN), the ZI is situated at a complex junction of major white matter pathways including the cerebellothalamic, pallidothalamic, medial lemniscal, and corticospinal tracts. Along its dorsal, ventral, and medial borders, the ZI is surrounded by the fasciculus thalamicus (ft; also known as the H1 field of Forel), the fasciculus lenticularis (fl; also known as the H2 field of Forel), and the H field, which is a convergence of the fl and the ansa lenticularis (al), respectively (Gallay et al., 2008; Nieuwenhuys, Voogd, & van Huijzen, 2007). The rostral ZI (rZI) is continuous with the reticular nucleus of the thalamus laterally and with the lateral hypothalamus anteromedially. The caudal ZI (cZI) is laterally bounded by the STN and posterior limb of the internal capsule. To date, most of the details regarding the region are the result of meticulous study of postmortem specimens (Gallay et al., 2008; Morel, 2007; Schaltenbrand & Wahren, 1977).

Cytoarchitectonic and myeloarchitectonic studies in experimental animals (most commonly rodents and primates) have identified the ZI as a gray matter complex consisting of loosely arranged neurons of heterogeneous morphology with a diverse immunohistochemical profile (Nieuwenhuys et al., 2007). In Golgi preparations of the ZI, two main neuronal classes have been identified: principal cells and interneurons (Ma, Johnson, & Hoskins, 1997). Gene expression studies have revealed a common embryological origin along with the reticular nucleus of the thalamus and pregeniculate nucleus of the ventral diencephalon, specifically the prethalamic segment, which predominantly contains GABAergic neurons (Puelles, Martínez-de-la-Torre, Ferran, & Watson, 2012; Watson, Lind, & Thomas, 2014). Through immunohistochemical analysis in experimental animals, a general pattern of at least four component ZI sectors has emerged in the rostral, dorsal, ventral, and caudal directions (Mitrofanis, 2005). Tract-tracing studies have identified extensive and often bilateral connections between the ZI and the cortex, subcortex, and spinal cord (Mitrofanis, 2005; Watson et al., 2014). At least five functional subsectors within the ZI have been suggested: auditory, limbic, motor, somatosensory, and visual. However, unlike other nearby structures like the STN, no robust immunohistochemical biomarker has been described for the ZI proper.

The diversity of chemical expression and widespread connections suggest an important modulatory role of the ZI in regulating brain function. The ZI forms extensive inhibitory connections with spinothalamic relay nuclei in rodents and nonhuman primates, and thus may play an important role in modulating neuropathic pain and the somatosensory system (Masri et al., 2009; Truini, Garcia-Larrea, & Cruccu, 2013). In a perhaps related manner, in rodent studies, the rostral ZI provides inhibitory control over the thalamus during sleep (Llinás & Jahnsen, 1982; Watson et al., 2014), which may also relate to its perceived role in modulating consciousness (Mitrofanis, 2005; Power & Mitrofanis, 2001). Finally, recent evidence, also in rodents, suggests an important role for the ZI in modulating fear generalization (Venkataraman et al., 2019) and appetite (Zhao et al., 2019).

In humans, the most well-studied role of the ZI is as a putative target for neuromodulatory therapy transmitted either within the cZI or its vicinity, which has been observed to be highly effective for the treatment of essential tremor (Hariz & Blomstedt, 2017). These investigations began in the 1960s with selective ablation (Bertrand, Hardy, Molina-Negro, & Martínez, 1969; Mundinger, 1965; Spiegel et al., 1962, 1964; Spiegel & Wycis, 1954; Velasco, Velasco, & Machado, 1975; Wertheimer, Lapras, & Levy, 1960), but as technologies improved, various groups (Blomstedt, Sandvik, & Tisch, 2010; Mohadjer, Goerke, Milius, Eto, & Mundinger, 1990; Nowacki et al., 2018; Plaha, Ben-Shlomo, Patel, & Gill, 2006; Velasco et al., 2001) demonstrated that electrical stimulation to these regions was also effective. Yet because of poor direct visualization, controversy has remained as to whether the therapeutic effect is derived from modulation of the cell bodies in the cZI, wayward connections such as the fasciculus cerebellothalamicus (fct; also known as the prelemniscal radiations or raprl) (Castro et al., 2015; Velasco, Molina-Negro, Bertrand, & Hardy, 1972), or some combination of both (Blomstedt et al., 2010). Given the ambiguity and high functional density of the region, the stereotactic target is often considered more broadly as the posterior subthalamic area (PSA; Blomstedt et al., 2018; Hariz & Blomstedt, 2017; Nowacki, Debove, et al., 2018). Targeting of the region relies on identification of the PSA indirectly relative to the adjacent STN and RN, which are visible on T2-weighted (T2w) scans (Blomstedt et al., 2010; Nowacki, Debove, et al., 2018).

The increased inherent signal resulting from increasing magnetic field strength has presented an opportunity to visualize brain structures that have not been seen at lower field strengths (DeKraker, Ferko, Lau, Köhler, & Khan, 2018; Marques & Norris, 2017). Many explorations of the deep brain at 7 T have exploited T2w tissue properties enabling visualization of many deep brain nuclei with improved resolution and signal-to-noise ratio (SNR) including the RN, substantia nigra, and STN (Keuken et al., 2013; Plantinga et al., 2018; Schäfer et al., 2012), known to be rich in iron (Haacke et al., 2005; Luigi, Youdim, Riederer, Connor, & Crichton, 2004). Paralleling these successes, previous attempts at direct visualization of the ZI have focused on the use of T2w contrast, with purported identification of the rZI, but not the cZI (Kerl et al., 2013). In this study, we report that, by employing high-resolution longitudinal (T1) mapping at 7 T, robust

visualization of the ZI and surrounding WM structures is possible *in vivo* along the entire rostrocaudal axis, allowing comprehensive anatomical characterization of this previously obscure deep brain region.

2 | MATERIALS AND METHODS

2.1 | Participant and image acquisition details

We recruited 32 healthy participants (46.2 ± 13.5 years; median: 48 years; range: 20–70 years; 12 female and 20 male; right-handed). This study was approved by the Western University Health Sciences Research Ethics Board (R-17-156). All subjects signed a written consent form to participate. The imaging studies were performed in a 7-T head-only scanner (Siemens Magnetom; Siemens Healthineers, Erlangen, Germany) at the Western University Centre for Functional and Metabolic Mapping (CFMM). An 8-channel parallel transmit/32-receive channel coil was used (Gilbert, Curtis, Gati, Klassen, & Menon, 2011). After localization and preparatory sequences, each subject underwent a 3D MP2RAGE (Marques et al., 2010), 3D SA2RAGE (Eggenschwiler, Kober, Magill, Gruetter, & Marques, 2012), and 3D optimized T2w fast-spin echo (T2 SPACE) acquisitions (see Table 1).

2.2 | Image preprocessing and template creation

Upon completion of an MRI scan session, the images were pushed to a DICOM server (dcm4che; <https://www.dcm4che.org>) with automatic data standardization and conversion to the Brain Imaging Data Structure (BIDS) (Gorgolewski, Auer, Calhoun, Craddock, & Das, 2016) using the autobids platform (<https://github.com/khanlab/autobids>) deployed on a high-performance compute cluster. Autobids uses scanner-specific heuristics enabled by heudiconv (<https://github.com/nipy/heudiconv>) preconfigured and validated on multiparametric 7 T MRI sequences for DICOM to nifti conversion using dcm2niix (Li, Morgan, Ashburner, Smith, & Rorden, 2016) and organization into BIDS.

All individual MRI sequences were corrected for gradient nonlinearities using 3D distortion correction (Glasser et al., 2013; Lau et al., 2018) prior to further processing. The objective of individual preprocessing steps was to adequately prepare the individual MRI sequences for quantitative image analysis and also linear alignment

with the subject's T1-weighted structural MRI scan containerized as BIDS apps (Gorgolewski et al., 2017). The outputs of the preprocessing steps were visually assessed for quality (J. L.).

2.2.1 | Preprocessing: MP2RAGE

As part of the MP2RAGE acquisition, two different images were created at separate inversions. Using a lookup table, these inversion images were used to create synthetic quantitative T1 maps devoid of proton density contrast, reception field bias, and first order transmit field (B_1^+) inhomogeneity. Minimal preprocessing was necessary except for using the B_1^+ field map (SA2RAGE) sequence to correct for intensity inhomogeneity (Eggenschwiler et al., 2012); specifically, no post hoc intensity nonuniformity correction was employed. This SA2RAGE-corrected T1 map was used for quantitative analysis. The T1w image was used as a reference image for rigid-body alignment of the T2SPACE scan.

2.2.2 | Preprocessing:T2SPACE

Raw images from the scanner were observed to have prominent intensity inhomogeneities, which were corrected using an initial non-uniformity correction step with N4 (Sled, Zijdenbos, & Evans, 1998; Tustison et al., 2010) enabling more accurate registration of the T1w image (and associated brain mask) to T2w. A synthetic T1-T2w fusion image was created by multiplying the T1w by the T2w image (Xiao, Fonov, et al., 2014) and re-estimating the intensity inhomogeneity again with N4. The original T2w image was denoised using the adaptive nonlocal means method (Manjón, Coupé, Martí-Bonmatí, Collins, & Robles, 2010) and the obtained inhomogeneity estimation was applied to the denoised image resulting in a final preprocessed T2w image in the scanner space. Rigid registration to the T1w scan was re-estimated using the preprocessed image. Final preprocessed images included both a T2w volume in the original scanner space as well as one resampled into the T1w structural space. The process was bootstrapped once after creating an initial T2w template (see Section 2.2.3) and using the template for histogram-based intensity normalization. Note that because of the combination of post hoc bias field correction and intensity normalization necessary to produce more homogeneous images, the per voxel values of the T2SPACE images are not directly comparable between scans in a quantitative

TABLE 1 MRI sequence details

Sequence	TE (ms)	TR (ms)	TI (ms)	Flip angle (°)	Matrix size	PAT ^a	Averages	Resolution (mm ³)	Acquisition time (s)
MP2RAGE	3D	2.73	6,000	800/2700	4/5	342 × 342 × 224	3	1	0.7 × 0.7 × 0.7
SA2RAGE	3D	0.81	2,400	45/1800	4/11	128 × 128 × 64	2	1	1.9 × 1.9 × 2.1
SPACE	3D	398	4,000	NA	Variable	320 × 320 × 224	3	1.6	0.7 × 0.7 × 0.7

^aPAT, parallel acquisition technique (acceleration factor).

manner. This processing pipeline has been released and containerized as a BIDS app (<https://github.com/khanlab/prepT2space/>).

2.2.3 | Template creation

The antsMultivariateTemplateCreation2 pipeline was used for multi-modal (T1,T2w) template creation (Avants et al., 2011). A corresponding T2w template (in T1 space) was created after propagating the participant T2w images to T1w template space using the relevant transformations produced using prepT2space. An initial template was created using rigid body alignment of each participant's T1w scan to the MNI2009bAsym template (0.5 mm isotropic resolution; Fonov, Evans, McKinstry, Almlí, & Collins, 2009). Over a series of 10 subsequent bootstrapped iterations, the deformable registration (diffeomorphic algorithm) was refined (shrink factors: $12 \times 6 \times 4 \times 2 \times 1$; smoothing factors: $6 \times 3 \times 2 \times 1 \times 0$ vox; max iterations: $100 \times 100 \times 70 \times 50 \times 10$; transformation model: Greedy SyN; similarity metric: cross-correlation). Using the derived affine and nonlinear transforms, the individual images (T1 and T2w) were transformed and resampled using trilinear interpolation into the template space. Mean intensity images were generated for each parametric sequence. The log Jacobian was computed, providing an estimate of local deformation required to transform each participant into the template space. The scripts for template creation have been archived for reference. Spatial correspondence was quantified using a recently described anatomical fiducial (AFID) placement protocol with residual AFID registration error (AFRE) being calculated across 32 validated anatomical features (Lau et al., 2019) (RRID:SCR_016623) placed in 3D Slicer (Fedorov et al., 2012) (RRID:SCR_005619). A mapping from our study specific 7 T template space to standard MNI coordinates (MNI2009bAsym) has also been provided to facilitate cross-study comparison.

2.3 | Region-of-interest segmentation

The ZI, RN, and STN were segmented using the 10th iteration T1 and T2w combined template using ITK-SNAP version 3.6.0. Each rater segmented the regions twice, with sessions spaced more than 2 weeks apart allowing us to calculate intra- and inter-rater reliability via the Jaccard and Dice coefficients. A representative template segmentation was derived by averaging all segmented ROIs and thresholding by majority voting (>50%)—this was considered the “gold” standard. Three raters segmented the RN and STN twice using the T2w image (J. D., J. L., Y. X.). We discovered that substructures of the zona incerta region were also visible, and thus, adopted the nomenclature of Morel (Morel, 2007) for describing the regional anatomy (see Table S1 for a glossary of terms and disambiguation). Caudally, the fasciculus cerebellothalamic (fct) and medial lemniscus (ml) could be delineated from the ZI. Rostrally, the fields of Forel, specifically the fasciculus thalamicus (ft or H1 field), fasciculus lenticularis (fl or H2 field), and medially the H field (hf) could also be identified.

Each of these structures was segmented twice (2 months apart) by the lead author using the T1 template. To our knowledge, these structures have not been previously segmented from *in vivo* images. As such, two stereotactic neurosurgeons (A. P., K. M.) were consulted throughout the ZI segmentation process: first, after the initial segmentations by the lead author (JL); second, after identifying critical boundaries of the ZI particularly rostrally; and finally, to review the final consensus segmentation. Several histological human brain atlases were used as references (Hawrylycz et al., 2012; Mai, Majtanik, & Paxinos, 2015; Morel, 2007; Schaltenbrand & Wahren, 1977). Consensus segmentations were propagated back into individual subject space using the deformations derived from the template creation step. Accurate spatial correspondence was confirmed by visual inspection by expert raters and also by determining that fiducial registration error was in the millimetric range (Figure 1 and Figure S2). Once consensus was achieved, manual segmentations were completed in five individual scans and voxel overlap measures using Jaccard and Dice were computed to assess the visibility of individual structures.

The rZI presented some challenges to accurate identification, not for lack of contrast, but due to difficulty with determining its relationship with the fl and ft. On close comparison with histological atlases, the fl appears to run through the rZI. We provide labels for the ZI as a whole, and provide separate labels for the rZI interposed fl, and cZI. Due to partial voluming, the lateral aspect of the central portion of the ZI (between rostral and caudal ends) was too thin to segment along its entire length in our dataset.

2.4 | Stereotactic target localization

Three clinicians (two neurosurgeons: K. M., A. P.; one senior neurosurgery resident: J. L.) placed target locations in the bilateral PSA according to two different placement schemes, which we refer to as Target01 (Blomstedt et al., 2010) and Target02 (Nowacki, Debove, et al., 2018) (Figure 4). Both schemes rely on anatomical targeting based on axial T2w images, after performing an initial AC-PC transformation using a validated technique (Lau et al., 2019) in 3D Slicer (Fedorov et al., 2012). Target01 involved the identification of the RN slice of maximal diameter, drawing a horizontal line to mark its equator. The boundary of the STN and its intersection with the RN equatorial line was approximated. Finally, a point was drawn half to two-thirds of the way along the point of STN/RN line intersection and the lateral border of the RN, marking the planned location of the electrode tip. Target02 involved the identification of three different lines: a horizontal line drawn along the equator of the RN identified on the axial slice of maximal diameter, an oblique line drawn along the long-axis of the STN, and finally, an oblique line perpendicular to the long-axis of the STN intersecting the lateral border of the RN at its equator. Consensus placements were agreed upon by the clinicians. The points were placed in the final template space and transformed into the individual participant space. Points in the individual participant space were qualitatively assessed for accuracy.

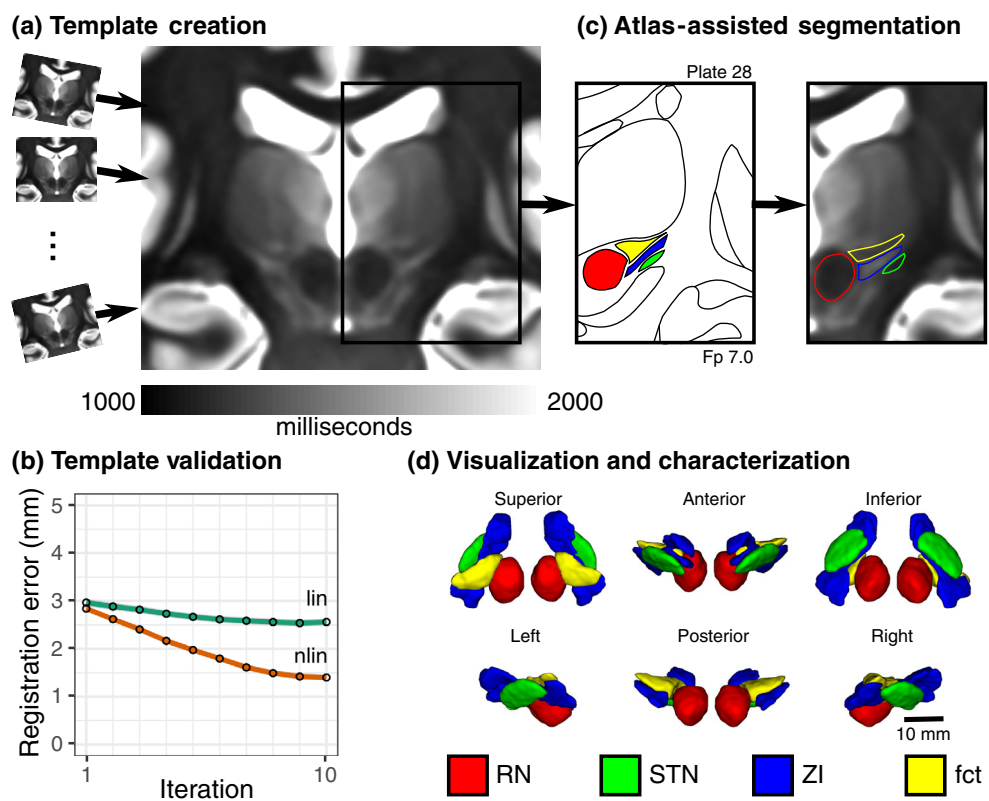


FIGURE 1 Study workflow for direct visualization and segmentation of the ZI region. (a) To visualize the ZI, we acquired 7 T1 maps from healthy participants. Individual subject data were pooled using deformable template creation methods to create a within-study population average. (b) Registration accuracy stabilized into the millimetric range with increasing complexity of registration (linear to nonlinear) and number of iterations (95% confidence intervals shown; details in Materials and Methods). (c) We found that thresholding our T1 maps to a specific range (1,000–2,000 ms) revealed similarities with conventional myelin-stained atlases, enabling segmentation of the ZI, demonstrated on Plate 28 (7 mm posterior to MCP) of the Schaltenbrand atlas (Schaltenbrand & Wahren, 1977), corresponding to Plate 48 of the Allen Brain THM Atlas (Hawrylycz et al., 2012) and Plate A6 of the Morel Atlas (Morel, Magnin, & Jeanmonod, 1997). Specifically, the ZI could be distinguished as separate from the fasciculus cerebellothalamicus (fct). Note: Equivalent T1 map images are shown to the left and right of the corresponding Schaltenbrand plate without and with segmentation overlay, respectively. (d) Once consensus segmentations were completed, the structures of the ZI were reconstructed in 3D. Note: the RN and STN labels were segmented based on the corresponding T2w images in this dataset

TABLE 2 MRI sequence details for study replication dataset

Sequence	TE (ms)	TR (ms)	TI (ms)	Flip angle (°)	Matrix size	PAT ^a	Averages	Resolution (mm ³)	Acquisition time (s)	
MP2RAGE	3D	2.47	5,000	900/2750	5/3	320 × 320 × 240	3	1	0.7 × 0.7 × 0.7	08:02
SA2RAGE	3D	0.78	2,400	45/1800	4/10	128 × 128 × 96	2	1	2 × 2 × 2	02:16

^aPAT, parallel acquisition technique (acceleration factor).

2.5 | Study replication

A second, independent dataset was included to study the inter-site replicability of our findings using age- and sex-matched participant data. This included MP2RAGE and SA2RAGE data acquired at the Maastricht University Brain Imaging Centre (MBIC, Maastricht, the Netherlands) using sequence parameters detailed in Table 2 and a 7-T whole-body MRI equipped with a single transmit, 32-channel receive head coil (Nova Medical, Wilmington, MA). Two dielectric pads containing a 25% suspension of barium titanate in deuterated water were placed proximal to the temporal lobe area to locally increase the

transmit B1+ field and to improve its homogeneity across the brain (Teeuwisse, Brink, Haines, & Webb, 2012). Ethical approval for the experimental procedures was provided by the local medical ethics committee (Maastricht University Medical Center, Maastricht, Netherlands). A total of 32 (cognitive) healthy and age-matched participants (46.6 ± 13.3 years; median: 48.5 years; range: 20–69 years; 17 females and 15 males) were included after obtaining written informed consent.

Analysis of the study replication dataset followed a similar workflow as outlined for the primary dataset, including B1+ correction of the MP2RAGE data and template building (see Section 2.2).

In addition, dielectric pads were removed from the images by intensity thresholding the second MP2RAGE inversion image to improve the subsequent template building process. Here, data from two subjects were discarded due to misregistration. Finally, the ZI, rZI, cZI, fct, and the ft segmentations obtained using the primary dataset (see Section 2.3) were projected onto the replication template by applying a primary-to-replication template registration to allow volumetry and relaxometry analyses in native subject space for evaluation of cross-study use of our segmentations. Manual segmentations were completed in five individual scans and voxel overlap measures were computed to assess the visibility of individual structures.

2.6 | Direct *in vivo* visualization at standard magnetic fields

Given our findings using high-resolution 7 T data, we investigated whether these features could similarly be visible at standard fields, which are more widely accessible. We explored several individual participant datasets using the DESPOT1 (Deoni, Peters, & Rutt, 2005) and MP2RAGE sequences at standard field. Furthermore, we investigated whether these features were visible on the ICBM MNI2009b template (Fonov et al., 2009) with appropriate windowing, which has been aligned with the BigBrain histological space (Amunts et al., 2013; Xiao et al., 2019).

3 | RESULTS

The 7 T MRI participant data were pooled using deformable template creation methods to create a within-study population average with validation of intersubject spatial correspondence (Lau et al., 2019) (Figure 1; registration accuracy: 1.27 ± 1.02 mm; Figure S2). The population average was reoriented relative to the anterior and posterior commissure allowing coordinates to be expressed relative to the mid-commissural point (MCP). The population averaging technique facilitated further boosting of the contrast and MRI measurements within the ZI region (Figure 1).

3.1 | Direct visualization of the human zona incerta and surrounding regions

With appropriate windowing, the contrast from the quantitative T1 maps was highly similar to classic myelin-stained histological atlas (Figure 1) (Schaltenbrand & Wahren, 1977) with white matter structures appearing hypointense relative to surrounding hyperintense gray matter. We found that the human ZI could be directly visualized *in vivo* along its entire rostrocaudal axis as a region of high T1 signal. Moreover, the ZI appeared distinct from the surrounding white matter tracts of the ft, fl, field H (fh), and medial lemniscus (ml) (Figure 1). Caudally, within the PSA, the fct could be clearly identified as a

distinctly identifiable region of relatively low T1 signal, anterior to the cZI and anterolateral to the RN, a structure previously only identified at high resolution on histological sections (Figures 1c, 4b, and 5). Rosstrally, regions of high T1 signal were identified both superior and inferior to the fl (Figure 2), leading us to identify an inferior/ventral rZI region ambiguously labeled in existing human atlases (Figure 3b). These substructures were not visible on T2w images.

3.2 | Characterization of the human zona incerta and surrounding regions

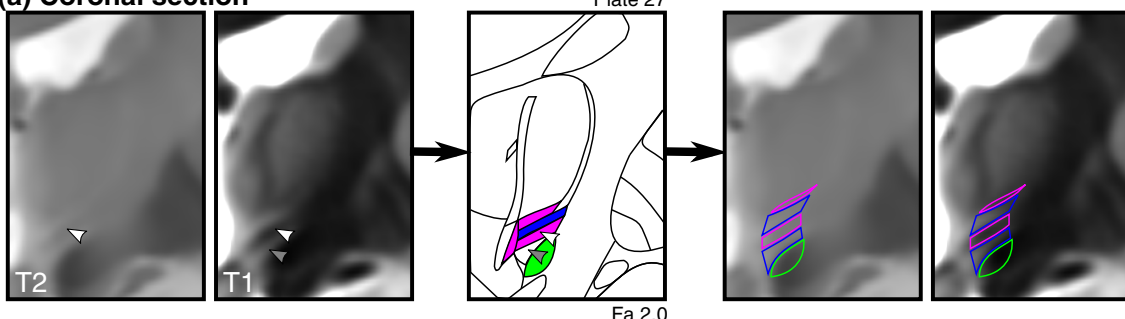
Direct visualization afforded us an opportunity to segment and characterize the human ZI morphologically using methods not previously possible (see Section 2 for details). The segmentations could generally be performed reliably (Dice scores >0.7) in both the template space and for individual datasets, with details provided in Table 3 and S3. As expected, manual segmentations could be performed more reliably in the template space. For individual subjects, the ZI, cZI, and rZI were segmented in individual subjects with a mean Dice score of 0.72, 0.76, and 0.68, respectively. The surrounding white matter structures (fct, fl, ft, hf, hfields, and ml) were segmented in individual subjects with a mean Dice score of 0.71, 0.63, 0.69, 0.71, 0.71, and 0.73, respectively. The STN and RN mean Dice scores were 0.91 and 0.78, respectively, consistent with previous studies.

Three-dimensional reconstructions permitted the identification of the ZI as an elongated band situated along the long axis of the STN with broader and more prominent components extending both rostrally and caudally (Figure 1d). To provide a sense of scale, the total volume described here represents a region with a bounding box of $20\text{ mm} \times 10\text{ mm} \times 10\text{ mm}$ or smaller than the tip of an adult human finger. Our analysis permitted the identification of concrete dimensions of the ZI, which spans on average approximately 20.4 mm along its main axis (rostrocaudally), 7.4 mm maximally along its secondary axis (medial to lateral), and varying in thickness from less than 1.0 mm along its lateral boundary to 3.6 mm in the cZI (Figure 1d). Calculations of rostral thickness were complicated by the wayward fl (see previous section; Figure 2), which if included, is as thick as 7.0 mm, whereas the dorsal rZI and ventral rZI have thickness of 3.7 and 1.8 mm, respectively when considered separately. The volume of the ZI was $252.4 \pm 22.4\text{ mm}^3$ with caudal and rostral components 83.6 ± 8.7 and $169.2 \pm 16.3\text{ mm}^3$, respectively.

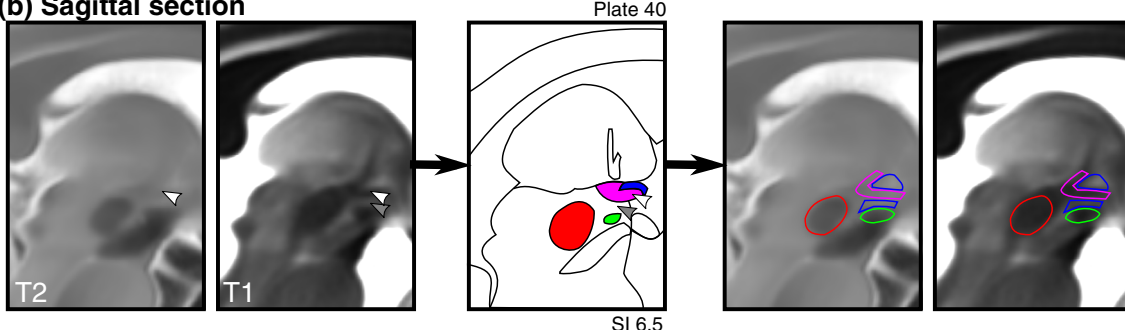
Morphological characterization could be extended to surrounding gray and white matter regions given they could also be well visualized. The RN and STN have been well-characterized in previous studies (Keuken et al., 2017; Xiao, Jannin, et al., 2014), providing anatomical boundaries to the ZI region with reliability consistent with prior studies (Tables S3a and S3b). Volumetric results were consistent with previous studies of the RN ($296.4 \pm 27.8\text{ mm}^3$) and the STN ($138.9 \pm 14.0\text{ mm}^3$). Of particular note, the fct was 12.2 mm along its longest axis, 5.4 mm (medial to lateral), and 5.0 mm thick maximally (medially) with a total volume of $135.7 \pm 13.3\text{ mm}^3$, similar in volume to the STN ($138.9 \pm 14.0\text{ mm}^3$),

Rostral zona incerta

(a) Coronal section



(b) Sagittal section



(c) 3D Reconstruction

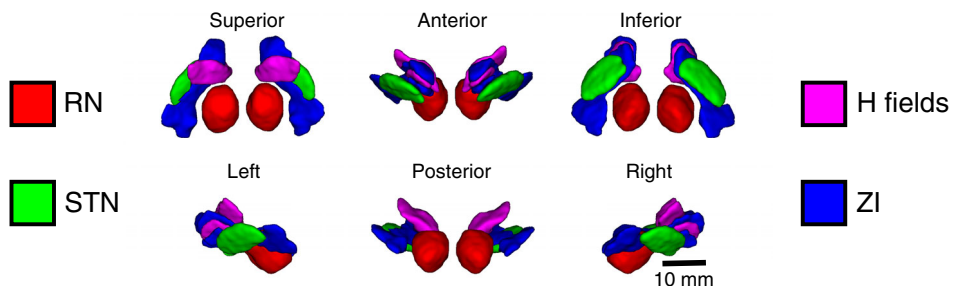


FIGURE 2 Direct visualization and segmentation of the rostral zona incerta including the fields of Forel. Select views of the rZI demonstrate separate dorsal and ventral components of the rZI as well as the H fields, which include the H1 field (fasciculus thalamicus), H2 field (fasciculus lenticularis), and H field. Equivalent MR images are shown to the left and right of the corresponding Schaltenbrand atlas plate without and with the segmentation overlay, respectively. (a) In the coronal plane, the white arrowhead demonstrates a T2w hypointense region previously identified as the rZI (Kerl et al., 2013). This location is relatively T1 hypointense, corresponding spatially and in terms of tissue characteristics to the myelinated H2 field (fl). Below this region (gray arrowhead) is an unlabeled T1 hyperintense region of the Schaltenbrand atlas (Plate 27; 2.0 mm anterior to MCP), corresponding to Plate 39 of the Allen Brain THM Atlas (Hawrylycz et al., 2012) and Plate A13 of the Morel Atlas (Morel et al., 1997). This location corresponds with the ventral rZI identified in other species (Mitrofanis, 2005). (b) These features are similarly identified in the sagittal view with a corresponding representative histological slice from Schaltenbrand (Plate 40, 6.5 mm lateral to MCP), corresponding to Plate L9.1 (6.3) of the Morel Atlas. Note: the Schaltenbrand atlas represents separate postmortem specimens in each cardinal orientation (coronal, sagittal, axial)

but located more posteriorly, and separated by the interposed gray matter of the middle to caudal ZI. The fields of Forel (ft, fl, field H) similarly could be distinguished from the rZI and separately segmented based on differences in T1 intensity with a total volume of $153.7 \pm 15.9 \text{ mm}^3$, also with a volume similar to the STN. The fl and ft tracts themselves formed concentrated bundles of around 1.2 mm diameter and could be distinguished anatomically as separate from the ZI with total volumes $52.0 \pm 5.7 \text{ mm}^3$ and 84.3 ± 8.8 ,

respectively, with the H field medially, consisting of the merger of the ft and al tracts (Gallay et al., 2008), being $54.6 \pm 5.7 \text{ mm}^3$. The locations of the structures in reference to the MCP (Table 4) were consistent with known values.

T1 measurements facilitated the identification of substructures of the ZI region in ways that T2w images did not (Table 4). Notably, in the main reported dataset, T1 values were robustly in the 1,200–1,300 ms range ($1,265.4 \pm 34.8 \text{ ms}$) in the ZI (Table 4 and

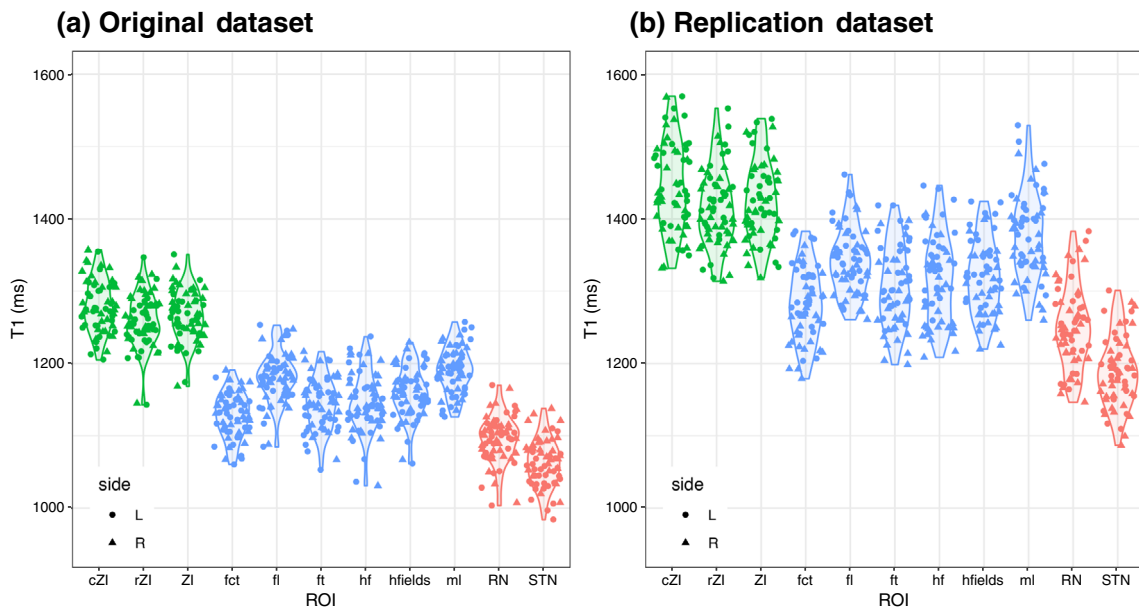


FIGURE 3 Distinct T1 values for different substructures of the zona incerta region as determined in our original dataset and a replication dataset. The general trends are the same with statistically significant differences in T1 values between the ZI (green) and surrounding white matter (blue) and gray matter (red) regions. The differences between datasets is an observed phenomenon from other studies related to inter-scanner differences and reviewed in Section 4 and a recent study (Haast et al., 2020). Although different, our analysis demonstrates that for a given scanner these tissue characteristics are relatively precise and allow the separation of these regional structures on the basis of local MRI characteristics alone

Figure 3). No differences in T1 values were found between the rZI and cZI (p -value n.s.). To examine whether peri-zonal substructures could be distinctly separated as suggested from our qualitative observations, we compared the T1 values in the ZI against the values in surrounding regions. Wilcoxon rank testing confirmed that T1 mapping was effective at distinguishing the ZI from surrounding local structures (Figure 3). The RN and STN had demonstrably shorter T1 times than the ZI ($1,094.9 \pm 32.7$ and $1,062.0 \pm 32.4$ ms, respectively; p -value $<.01$). The surrounding white matter tracts were also clearly separable from the ZI, despite their small size, due to distinctly shorter T1 times. Such tracts include the fields of Forel, the fl inferiorly (volume: 52.0 ± 5.7 mm 3 ; T1: 1180.2 ± 34.4 ms, $p < .01$) and the fascicularis thalamicus (ft) superiorly (volume: 84.3 ± 8.8 mm 3 ; T1: 1143.1 ± 35.1 ms, $p < .01$). The fct was also distinct from the ZI (volume: 252.4 ± 22.4 mm 3 ; T1: 1127.9 ± 30.5 ms), which is of relevance to known surgical neuromodulatory targets.

These analyses were repeated in a matched dataset from Maastricht University (see Section 2; collaborators: R.H. and K.U.). Wilcoxon rank sum testing again confirmed intensity differences between the ZI and neighboring white matter and gray matter structures (p -value $<.01$). These results are reported in detail in the associated notebook provided on GitHub. Although the exact T1 values differed (Figure 3), intra-regional variability in T1 was comparably low across datasets (Figure 3b). These inter-scanner differences are a known phenomenon explored in a recent study (Haast et al., 2020).

3.3 | Direct evaluation of indirect surgical targets of the zona incerta region

Surgical targets of the ZI region have conventionally been targeted indirectly and the specific area that results in a therapeutic effect remains controversial. We used the high-resolution combined T1 and T2w *in vivo* maps reported in this study to directly evaluate two conventional indirect targets located in the ZI region. Specifically, the PSA is targeted using features from T2w contrast based on the relative positions of the STN and RN. We have demonstrated that the cZI and fct can be separated on the basis of both anatomical location and underlying T1-based tissue characteristics. Two commonly described indirect targets, here referred to as Target01 (Blomstedt et al., 2010) and Target02 (Nowacki, Debove, et al., 2018), were placed on T2w images, allowing us to evaluate to which feature (or features) this best corresponded on our T1 maps (Figure 4).

The target placements anatomically corresponded to the boundary between the cZI and the fct lateral to the ipsilateral RN (Figure 4c). This observation was quantitatively supported by our finding that mean T1 values at the surgical targets were lower than in the cZI for both Target01 and Target02 (Figure S4c; Wilcoxon rank sum testing $p < .05$), but higher than values in the fct. We also calculated the distance between each indirectly placed target and separately the centroid of the ipsilateral fct and cZI, and assessed whether the indirect target was closer to one or the other. Target01 was almost equidistant from the cZI and fct (3.30 ± 0.22 vs. 3.46 ± 0.27 mm, respectively), while Target02 was further from cZI and closer to fct (4.62 ± 0.36 vs.

TABLE 3 Summary of voxel overlap measures for manual segmentations of the original and replication dataset

		Template segmentation		Individual subject segmentation			
Region	Side	Original dataset		Original dataset		Replication dataset	
		Jaccard	Kappa	Jaccard	Kappa	Jaccard	Kappa
cZI	L	0.88 ± 0.01	0.94 ± 0.01	0.63 ± 0.04	0.77 ± 0.03	0.64 ± 0.04	0.78 ± 0.03
	R	0.84 ± 0.02	0.91 ± 0.01	0.59 ± 0.02	0.74 ± 0.02	0.59 ± 0.04	0.74 ± 0.03
	Combined	0.86 ± 0.03	0.93 ± 0.02	0.61 ± 0.03	0.76 ± 0.03	0.62 ± 0.05	0.76 ± 0.04
fct	L	0.80 ± 0.14	0.89 ± 0.09	0.55 ± 0.01	0.71 ± 0.01	0.53 ± 0.03	0.69 ± 0.03
	R	0.80 ± 0.14	0.88 ± 0.08	0.55 ± 0.01	0.71 ± 0.01	0.56 ± 0.06	0.72 ± 0.05
	Combined	0.80 ± 0.11	0.89 ± 0.07	0.55 ± 0.01	0.71 ± 0.01	0.55 ± 0.05	0.71 ± 0.04
fl	L	0.76 ± 0.15	0.86 ± 0.09	0.45 ± 0.02	0.62 ± 0.02	0.46 ± 0.07	0.63 ± 0.07
	R	0.79 ± 0.14	0.88 ± 0.09	0.47 ± 0.02	0.64 ± 0.01	0.45 ± 0.07	0.61 ± 0.07
	Combined	0.77 ± 0.12	0.87 ± 0.08	0.46 ± 0.02	0.63 ± 0.02	0.45 ± 0.07	0.62 ± 0.07
ft	L	0.79 ± 0.01	0.89 ± 0.01	0.53 ± 0.03	0.69 ± 0.02	0.47 ± 0.07	0.63 ± 0.07
	R	0.80 ± 0.03	0.89 ± 0.02	0.52 ± 0.02	0.68 ± 0.02	0.48 ± 0.08	0.64 ± 0.07
	Combined	0.80 ± 0.02	0.89 ± 0.01	0.53 ± 0.02	0.69 ± 0.02	0.47 ± 0.07	0.64 ± 0.07
hf	L	0.79 ± 0.06	0.88 ± 0.04	0.55 ± 0.04	0.71 ± 0.04	0.53 ± 0.07	0.69 ± 0.06
	R	0.79 ± 0.07	0.88 ± 0.04	0.56 ± 0.01	0.72 ± 0.01	0.55 ± 0.05	0.71 ± 0.04
	Combined	0.79 ± 0.06	0.88 ± 0.03	0.55 ± 0.03	0.71 ± 0.03	0.54 ± 0.06	0.70 ± 0.05
hfields	L	0.81 ± 0.04	0.89 ± 0.02	0.55 ± 0.02	0.71 ± 0.02	0.53 ± 0.05	0.69 ± 0.04
	R	0.82 ± 0.03	0.90 ± 0.02	0.56 ± 0.02	0.72 ± 0.01	0.54 ± 0.04	0.70 ± 0.04
	Combined	0.81 ± 0.03	0.90 ± 0.02	0.56 ± 0.02	0.71 ± 0.02	0.53 ± 0.04	0.70 ± 0.04
ml	L	0.82 ± 0.20	0.89 ± 0.12	0.57 ± 0.02	0.72 ± 0.02	0.52 ± 0.05	0.68 ± 0.04
	R	0.86 ± 0.01	0.92 ± 0.01	0.58 ± 0.02	0.74 ± 0.02	0.53 ± 0.08	0.69 ± 0.07
	Combined	0.84 ± 0.12	0.91 ± 0.07	0.58 ± 0.02	0.73 ± 0.02	0.53 ± 0.06	0.69 ± 0.05
rZI	L	0.78 ± 0.14	0.87 ± 0.09	0.51 ± 0.02	0.68 ± 0.01	0.52 ± 0.04	0.68 ± 0.03
	R	0.79 ± 0.11	0.88 ± 0.07	0.51 ± 0.01	0.67 ± 0.01	0.51 ± 0.05	0.68 ± 0.04
	Combined	0.78 ± 0.11	0.88 ± 0.07	0.51 ± 0.01	0.68 ± 0.01	0.52 ± 0.04	0.68 ± 0.04
ZI	L	0.83 ± 0.09	0.91 ± 0.05	0.56 ± 0.01	0.72 ± 0.01	0.57 ± 0.03	0.73 ± 0.03
	R	0.83 ± 0.08	0.90 ± 0.05	0.55 ± 0.01	0.71 ± 0.01	0.55 ± 0.05	0.71 ± 0.04
	Combined	0.83 ± 0.07	0.91 ± 0.04	0.56 ± 0.01	0.72 ± 0.01	0.56 ± 0.04	0.72 ± 0.04
RN ^a	L	0.95 ± 0.03	0.98 ± 0.02	0.82 ± 0.05	0.90 ± 0.03		
	R	0.95 ± 0.03	0.98 ± 0.01	0.84 ± 0.02	0.91 ± 0.01		
	Combined	0.95 ± 0.03	0.98 ± 0.01	0.83 ± 0.04	0.91 ± 0.02		
STN ^a	L	0.90 ± 0.10	0.94 ± 0.06	0.64 ± 0.06	0.78 ± 0.04		
	R	0.89 ± 0.10	0.94 ± 0.05	0.65 ± 0.03	0.78 ± 0.02		
	Combined	0.89 ± 0.10	0.94 ± 0.05	0.64 ± 0.04	0.78 ± 0.03		

^aThe RN and STN were segmented using the T2w scan, which was not acquired in the replication dataset.

2.64 ± 0.52 mm, respectively). Differences were confirmed using Wilcoxon rank testing ($p < 0.01$; Figures S4a and S4b). The ability to separate the fct from the cZI is demonstrated pictorially in a montage of all participant data (Figure 5) as well as quantitatively (Figure 3).

3.4 | The zona incerta region at standard magnetic field strength

Motivated by our discovery at 7 T, we investigated whether we could identify a similar feature at standard magnetic fields, given that they

are more widely accessible. Indeed, we determined that on individual T1 map datasets at 3T, a region of relative hypointensity could be seen that represents the gray matter regions of the ZI (Figure 6a). Thus, for practical purposes, a properly optimized T1 map protocol may be sufficient for identification of the nuclear region. In addition, we determined that the ZI is visible on T1w images as a relatively hypointense feature (Figure 6b), when windowed, although the windowing values themselves are arbitrary. Finally, we transformed our regions into the MNI2009bAsym space for use by other groups, which has the advantage of also having close correspondence with the BigBrain template (Xiao et al., 2019).

TABLE 4 Summary of volume, T1 values, and location relative to the MCP for the zona incerta and surrounding structures

Region	Side	Volume (mm ³)	T1 (ms)	Coordinates (mm)		
				x	y	z
cZI	L	87.4 ± 8.1	1,272.9 ± 34.7	-12.42 ± 0.78	-8.04 ± 1.15	-5.16 ± 1.18
	R	79.8 ± 7.6	1,286.6 ± 36.5	12.59 ± 0.81	-7.68 ± 1.21	-5.12 ± 1.09
	Combined	83.6 ± 8.7	1,279.7 ± 36.0			
rZI	L	168.7 ± 16.6	1,250.4 ± 36.8	-6.97 ± 0.54	1.69 ± 0.53	-0.79 ± 0.53
	R	169.8 ± 16.3	1,266.0 ± 36.9	7.11 ± 0.61	2.44 ± 0.61	-0.88 ± 0.59
	Combined	169.2 ± 16.3	1,258.2 ± 37.4			
ZI ^a	L	254.3 ± 22.5	1,258.6 ± 34.4	-8.82 ± 0.56	-1.61 ± 0.63	-2.27 ± 0.52
	R	250.6 ± 22.5	1,272.3 ± 34.5	8.86 ± 0.61	-0.81 ± 0.73	-2.28 ± 0.46
	Combined	252.4 ± 22.4	1,265.4 ± 34.8			
fct	L	136.0 ± 12.8	1,120.5 ± 30.5	-10.24 ± 0.68	-5.24 ± 0.78	-2.11 ± 0.83
	R	135.4 ± 14.0	1,135.3 ± 29.1	10.00 ± 0.67	-4.83 ± 0.88	-2.62 ± 0.73
	Combined	135.7 ± 13.3	1,127.9 ± 30.5			
fl	L	51.8 ± 5.9	1,178.9 ± 34.9	-6.09 ± 0.56	3.36 ± 0.50	-0.49 ± 0.65
	R	52.2 ± 5.6	1,181.4 ± 34.5	6.65 ± 0.64	3.81 ± 0.63	-0.51 ± 0.76
	Combined	52.0 ± 5.7	1,180.2 ± 34.4			
ft	L	84.0 ± 9.2	1,135.2 ± 35.6	-7.24 ± 0.59	-0.12 ± 0.60	1.31 ± 0.43
	R	84.5 ± 8.6	1,150.9 ± 33.4	7.58 ± 0.69	0.39 ± 0.73	1.14 ± 0.46
	Combined	84.3 ± 8.8	1,143.1 ± 35.1			
hf	L	53.4 ± 5.5	1,142.8 ± 41.8	-5.00 ± 0.47	-0.08 ± 0.52	-1.24 ± 0.38
	R	55.7 ± 5.6	1,148.2 ± 40.9	5.13 ± 0.53	0.39 ± 0.62	-1.28 ± 0.42
	Combined	54.6 ± 5.7	1,145.5 ± 41.1			
hfields ^b	L	153.4 ± 16.2	1,154.1 ± 35.0	-6.46 ± 0.55	1.13 ± 0.53	0.29 ± 0.46
	R	154.0 ± 15.8	1,162.2 ± 34.1	6.83 ± 0.63	1.55 ± 0.65	0.16 ± 0.51
	Combined	153.7 ± 15.9	1,158.1 ± 34.5			
ml	L	38.6 ± 3.8	1,188.4 ± 34.6	-9.04 ± 0.73	-10.58 ± 0.91	-3.39 ± 1.42
	R	29.2 ± 3.0	1,192.2 ± 27.7	8.96 ± 0.77	-10.14 ± 1.03	-3.40 ± 1.31
	Combined	33.9 ± 5.8	1,190.3 ± 31.2			
RN	L	292.1 ± 27.1	1,093.2 ± 33.4	-4.56 ± 0.48	-5.92 ± 1.05	-6.56 ± 0.89
	R	300.7 ± 28.3	1,096.6 ± 32.4	4.53 ± 0.52	-5.65 ± 1.09	-6.54 ± 0.84
	Combined	296.4 ± 27.8	1,094.9 ± 32.7			
STN	L	144.2 ± 13.3	1,045.8 ± 27.3	-10.00 ± 0.66	-0.47 ± 0.79	-3.15 ± 0.57
	R	133.6 ± 12.7	1,078.2 ± 29.2	10.23 ± 0.70	-0.01 ± 0.88	-3.29 ± 0.57
	Combined	138.9 ± 14.0	1,062.0 ± 32.4			

^aIncludes rZI and cZI.^bIncludes fl, ft, hf.

4 | DISCUSSION

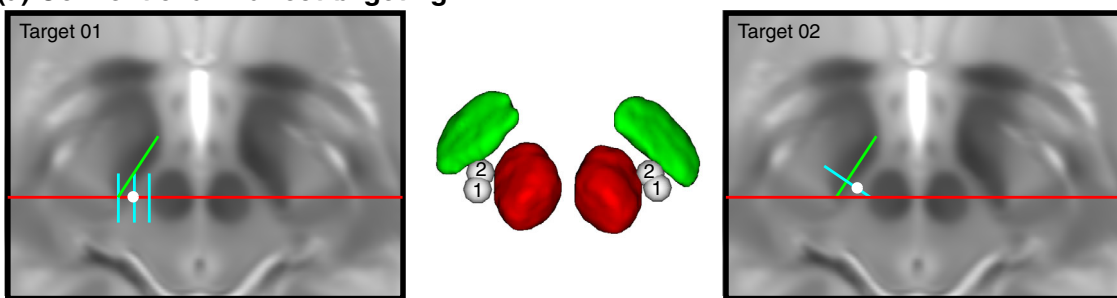
The present study demonstrates that robust visualization of the ZI and surrounding structures is possible using high-resolution quantitative T1 mapping. We report the first precise delineation of the ZI region *in vivo* providing estimates of the morphology (volume and dimensions) and T1 values. We found that the T1 relaxometry parameters of the ZI were distinct from surrounding white matter pathways. This finding enabled us to decouple a component of the rZI as separate and inferior to the fascicularis lenticularis, which to our

knowledge has not previously been labeled on histological atlases of the human brain (Figure 2). Due to the striking similarity in tissue contrast with classic postmortem myelin staining, we were able to segment the fct as a substructure within the PSA separate from the cZI. This methodology was then used for prospective identification of the active stimulation location for deep brain stimulation for which current standard-of-care relies on indirect targeting.

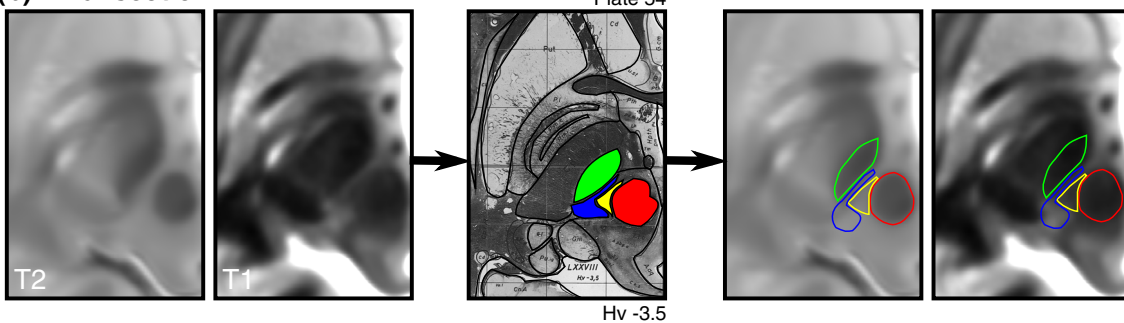
Efforts at visualizing small structures of the deep brain using high-field MRI have mostly focused on T2w relaxation properties due to the high paramagnetic contrast produced by many

Caudal zona incerta / posterior subthalamic area

(a) Conventional indirect targeting



(b) Axial section



(c) Comparing direct visualization with indirect targeting

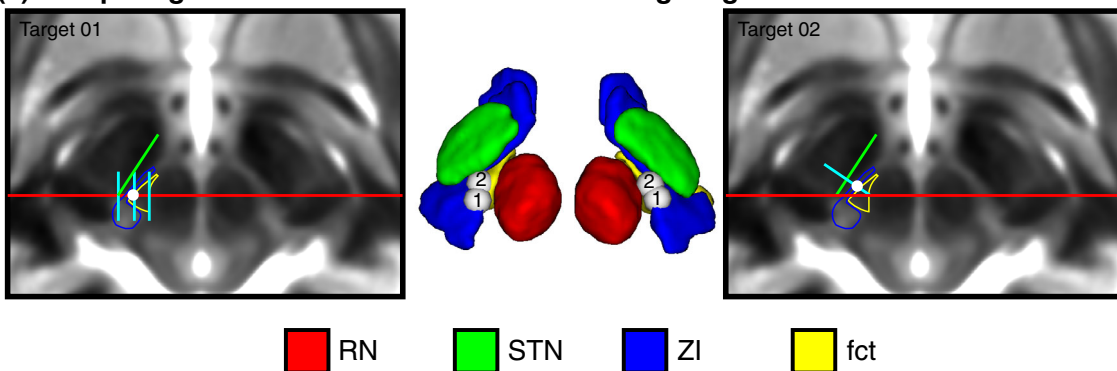


FIGURE 4 Direct visualization of conventional indirect targets of the posterior subthalamic area. (a) Two conventional indirect targeting methods, Target01 (Blomstedt et al., 2010) and Target02 (Nowacki, Debove, et al., 2018), used for stereotactic targeting in the PSA based on the relative location of the RN and STN at the level of the maximal diameter of the RN. (b) Using the Schaltenbrand atlas as a reference (Plate 54, 3.5 mm below MCP), also corresponding to Plate V2.7 of the Morel atlas, we identified the cZI and fasciculus cerebellothalamicus (fct) using the T1 maps (thresholded between 1,000–2,000 ms). Equivalent MR images are shown to the left and right of the corresponding Schaltenbrand atlas plate without and with the segmentation overlay, respectively. (c) Using the T1 map as an underlay image for our indirect targets provides additional detail regarding the location of the target relative to the cZI and fct, demonstrating that the targets are at the boundary between the two structures. Note: the 3D reconstructions represent an inferior surface view of the ZI region, which best depicts the location of the targets relative to the surrounding structures

subcortical nuclei due to endogenous ferritin (Haacke et al., 2005; Rudko et al., 2014; L. Zecca et al., 2004). Increasing the strength of the main magnetic field (B_0) results in an at least linear increase in signal, a two- to threefold increase compared to conventional clinical field strengths. This increased signal can be exploited in a number of ways, including higher resolution (submillimetric) imaging. Visualization at high fields has led to more robust imaging of small structures including the STN and SN using T2w contrast mechanisms (Keuken et al., 2013). The ZI has proven to be elusive to

visualization using T2w contrast. In one study at 7 T, using a T2w sequence, the rostral but not the cZI was reported as visible (Kerl et al., 2013), which we demonstrate is actually the fl (Figure 2). As a result, protocols for stereotactic targeting of the cZI have relied on the relative visibility of the surrounding RN and STN, from which the location of the stereotactic target within the PSA could be indirectly inferred. Overall, our results confirm that the ZI is not a strong generator of T2w contrast and led us to explore other potential generators of MR contrast.

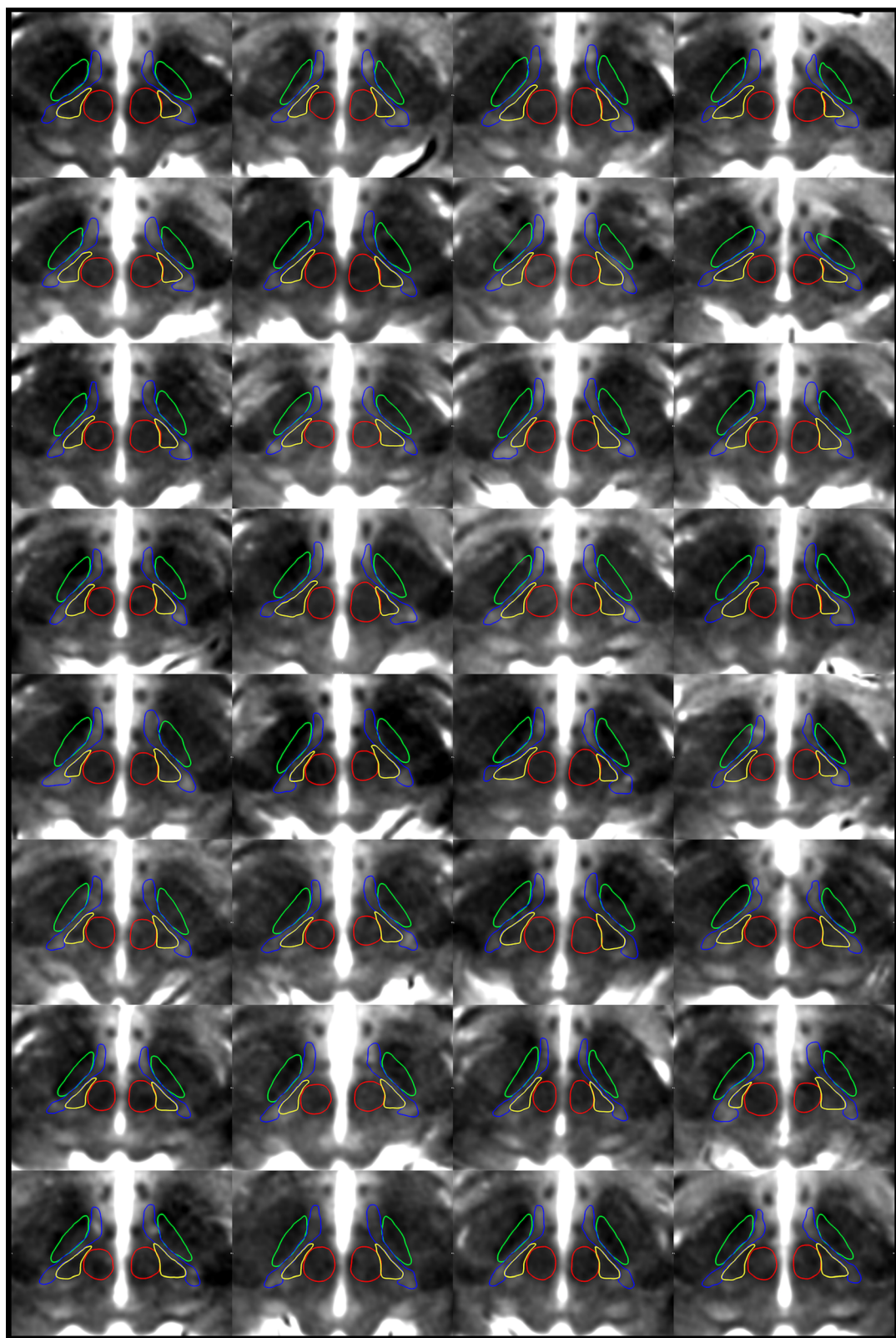


FIGURE 5 Montage of participant data demonstrating the ability to delineate the zona incerta substructures using high-resolution T1 maps. Representative axial slices demonstrate the ability to distinguish between the fct (yellow) and ZI (blue) at the level of the RN (red) for each individual participant ($N = 32$). Note the RN and STN (green) were initially segmented using the T2w images for the same subject fused into T1 space. The T1 maps are thresholded between 1,000–2,000 ms

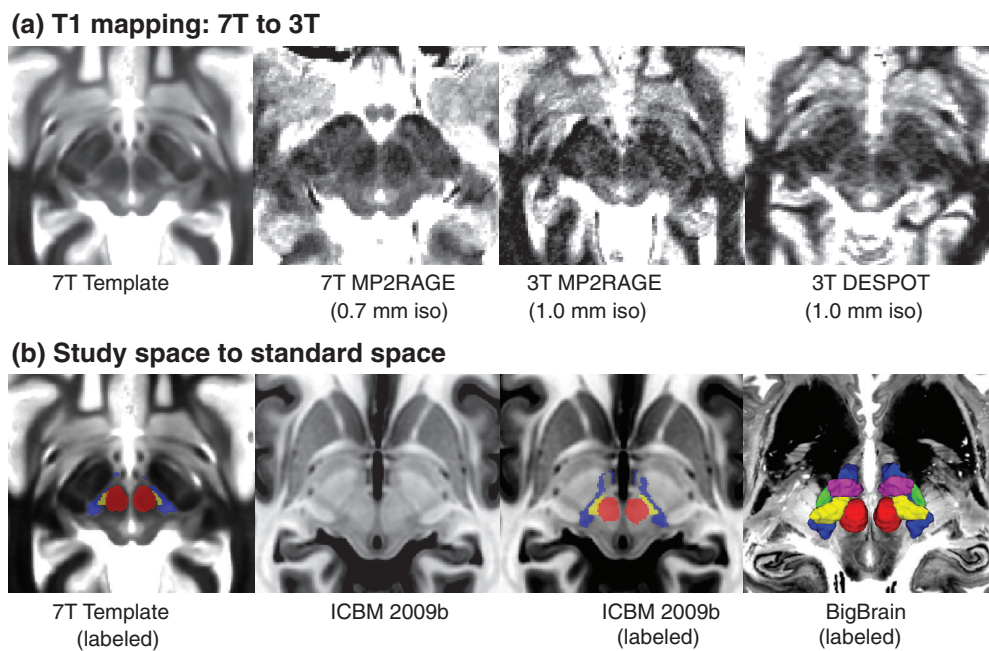


FIGURE 6 Implications for standard magnetic field strengths and standard spaces. (a) Based on our findings, we investigated whether the ZI substructures could be visualized at standard magnetic field strength. Based on our qualitative assessment, the cZI could be well visualized even at 3T using two different techniques (1.0 mm isotropic resolution, compared to 0.7 mm isotropic resolution at 7 T). (b) The ZI subregions created in this study have been transformed into ICBM 2009b space to benefit the neuroscience community. Note that on the T1w ICBM 2009b template, the cZI appears as a hypointense region while the fasciculus cerebellothalamicus is relatively hyperintense (inverse of T1 map). However, the units in the ICBM space are arbitrary. The 3D reconstructions are overlaid on top of the BigBrain template (Amunts et al., 2013; Xiao et al., 2019)

In the present study, we found that T1 rather than T2w relaxation properties of the ZI better delineated the substructures in the region. T1 relaxation times increase in a field-dependent manner, as does the dispersion between brain tissue types (Rooney et al., 2007), which have the effect of improving contrast between tissue types at 7 T. This advantage has been exploited to parcellate thalamic nuclei (Tourdias, Saranathan, Levesque, Su, & Rutt, 2014) and investigate cortical laminae (Trampel, Bazin, Pine, & Weiskopf, 2017). Surgical planning and in vivo histology have been considered important potential applications of the MP2RAGE sequence (Marques et al., 2010; Marques & Gruetter, 2013). In fact, using this method, we demonstrate that the ZI can also be visualized along its entire rostrocaudal axis (Figure 1). Furthermore, we found sufficient difference in T1-related tissue parameters to permit separation of the cZI from surrounding white matter tracts, including the fct of the PSA and the fields of Forel (ft and fl) from the rZI (Figure 2). Rostrally, these contrast differences permitted more detailed characterization of the relationship between the fl and rZI, dividing the rZI into dorsal and ventral components described in experimental animals (Mitrofanis, 2005; Watson et al., 2014) and one human brain atlas (Mai et al., 2015). Although the increase in T1 tissue values with field strength has been perceived as a disadvantage due to increased scan time, our results indicate that sufficient resolution and contrast can be attained within a clinically reasonable timeframe.

Since the boundaries of the ZI have not previously been well-defined in three dimensions, consensus segmentations were

performed using group averaging to further boost the SNR when delineating these structures. Our interpretation of the boundaries of the ZI using *in vivo* sequences was based on detailed comparison with annotations of the ZI from classical and modern histological sections (Hawrylycz et al., 2012; Mai et al., 2015; Morel, 2007; Schaltenbrand & Wahren, 1977). The majority of the segmented structures in the ZI region could be reliably segmented in both the template space and for individual scans (Dice >0.70 being considered reliable) although segmentation of the rZI, fl, and ft in individual subjects was less reliable (Table 3). Dice scores are generally lower for smaller structures, as small random errors in the boundary have a larger relative weight when volumes are smaller. For the rZI, the complex morphology of this region and its relationship with the white matter tracts of the fields of Forel is likely another contributing factor. Whether to include the newly identified (and previously unlabeled) region between H2 and the STN also likely increased uncertainty of segmentation of the rZI. We opted via consensus to include this in the definition of the rZI although this will have to be investigated in future studies integrating histology and other methods. For the fl and ft the decreased reliability likely relates to the small size of these structures (50 and 80 mm^3) as well as the challenge of identifying the lateral limits of segmentation given that they are white matter structures projecting to other nuclei. To compute estimates across the study population, the template segmentations were propagated back to the individual datasets using the transformations computed during the template creation process. This template creation approach allowed for the pooling of data from

multiple participants ($N = 32$) into a single reference space allowing us to better account for intersubject variability. Compared to histological evaluations, our approach enables high-resolution imaging without the drawbacks of histological processing, which include tissue deformations, processing artifacts, and other technical issues (Morel, 2007; Nowacki et al., 2018).

Our analysis demonstrates that there is sufficient signal and contrast within the PSA region to allow separation of the cZI from the fct (see Table 4). We discovered that commonly used T2w indirect anatomical target and optimal stimulation locations appeared at the boundary of the cZI with the PSA (Figures 4 and S4). These findings are in line with other work suggesting that a proportion of benefit is derived from stimulation of wayward white matter tracts in the fct (raprl) (Blomstedt et al., 2018; Mohadjer et al., 1990; Mundinger, 1965; Spiegel et al., 1964; Velasco et al., 1972), and also concordant with recent studies employing diffusion tensor imaging (DTI) (Dallapiazza et al., 2018; Dembek et al., 2019; Fenoy & Schiess, 2017; Fiechter et al., 2017; Sammartino et al., 2016; Velasco, Esqueda-Liquidano, Velasco, & García-Gomar, 2018). Compared to DTI-based measures, ultra-high field T1 mapping has higher SNR, is less prone to image distortions, require generally less scan time, less post-processing, and is acquired at inherently higher resolution (0.7 mm isotropic compared to 2–3 mm). We have determined that the dimensions of the fct within the PSA is ~4–5 mm along its longest axis, representing 1–3 voxels if relying on DTI alone compared to 5–7 voxels using our protocol. Direct visualization presents the possibility of submillimetric to millimetric level refinement of the therapeutic target and stimulation parameters, particularly if newer current steering devices are implanted.

Our findings add to the growing body of knowledge that the optimal DBS target within the PSA is at the anterior boundary of the cZI abutting or directly within the fct (Fiechter et al., 2017; Herrington, Cheng, & Eskandar, 2016). This suggests that direct targeting of the white matter, in other words connection-based targeting, may be central to efficacy, which has increasingly been acknowledged for essential tremor (Akram et al., 2018; Al-Fatly et al., 2019) and other disorders (Horn et al., 2017). Our approach using T1 mapping for visualizing local WM tracts might be considered divergent from recent approaches using diffusion-based imaging. With respect to human *in vivo* studies, DTI studies have mostly focused on connections between larger cortical and subcortical structures since achieving high resolution (submillimetric) images in clinically feasible timeframes for DTI remains a challenge. There is also increasing acknowledgement that connectivity-based methods are prone to producing false-positive tracts (Maier-Hein et al., 2017). An additional advantage of using T1 mapping, is that the images can simultaneously be used as a baseline structural scan and furthermore used to identify the target, eliminating the need for an image fusion step, which can introduce error. Ultimately, the approach taken here, particularly with increasingly higher resolution imaging, should be considered complementary to diffusion-based endeavors, enabling accurate localization of smaller tracts and structures using a multi-contrast approach. For example, anatomical segmentations of local white matter tracts at the template

and individual participant levels could be used to optimize tractographic and connectomic approaches, as seed regions to boost sensitivity to smaller tracts.

Some discrepancy in T1 map values was noted when comparing values reported between sites (Figure 3b) and studies (Forstmann et al., 2014; Keuken et al., 2017). In particular, our values tended to be ~100–200 ms shorter within the STN and SN. Ideally, quantitative maps should be independent of imaging sites and scanner vendors, and indicative of underlying tissue parameters. However, several factors may account for discrepancies between studies employing comparable quantitative imaging approaches (Stikov et al., 2015). For quantitative T1 mapping, the inversion recovery (IR) method is traditionally considered the gold standard (Drain, 1949; Hahn, 1949). However, several limitations, including long scan times associated with the acquisition of many images, reduce its utility for practical purposes. Therefore, more time efficient methods like the DESPOT (Deoni et al., 2005) and MP2RAGE (Marques et al., 2010) sequences have gained significantly in popularity in the last decade, with the latter being commonly acquired for higher field strength T1 mapping. In contrast to the traditional IR approach, the MP2RAGE approach requires the acquisition of only two images at different inversion times, which due to the interleaved nature of the sequence are inherently co-registered. This limits the effect of subject motion on the precision to map T1 and delineation of subcortical regions. In addition, whereas more conventional anatomical sequences applied in the clinic are influenced by M0 (i.e., proton density), T2*, B1- (i.e., radio-frequency [RF] receive) and B1+ (i.e., transmit) fields, the MP2RAGE approach removes these effects by only varying the inversion time and flip angles between each inversion image. However, we have recently shown that the slight variations in MP2RAGE setup between the original and replication datasets can introduce strong variability of cortical T1 across the brain, with observed differences leading up to 260 ms between datasets (Haast et al., 2020). These differences are most presumably related to differences in their sensitivity to B1+ inhomogeneities as post hoc B1+ correction (Eggenschwiler et al., 2012; Marques & Gruetter, 2013) lowered inter-dataset offsets to under 100 ms for both cortical (Haast et al., 2020), as well as subcortical T1 (this paper). Moreover, inter-scanner variability in hardware—our use of parallel versus single RF transmission for tissue excitation—may amplify this B1+ sensitivity. In addition, the differences in acquisition parameters (Table S5) can introduce additional sequence-dependent measurement variability due to assumptions about mono-exponential T1 relaxation in the MP2RAGE implementation (Roux, Levesque, & Rutt, 2016). Although differences in T1 are observed between the original and replication datasets, a striking correspondence is visible in terms of the relative T1 values between assessed regions proving the value of T1 mapping to identify these regions in a time efficient manner. Finally, how the findings in this study hold in the presence of pathology or atrophy remains an unanswered question and will be the subject of future work.

5 | CONCLUSIONS

In the present study, we demonstrate that direct *in vivo* visualization of the structures of the human ZI region is possible, a region originally described as an “immensely confusing area about which nothing can be said.” We successfully derived estimates of the size, shape, location, and tissue characteristics of substructures in the peri-zonal region noninvasively at high (submillimetric) resolution. Our findings confirm observations, only previously possible through histological evaluation, that the ZI is not simply a space between structures but contains distinct morphological entities that should be considered separately. Our findings pave the way for increasingly detailed *in vivo* study and provide a structural foundation for precise functional and neuromodulatory investigation bringing increasing certainty to this uncertain area.

ACKNOWLEDGMENTS

Jonathan C. Lau is funded through the Western University Clinical Investigator Program accredited by the Royal College of Physicians and Surgeons of Canada and a CIHR Frederick Banting and Charles Best Canada Graduate Doctoral Award Scholarship. Kamil Uludag was supported by a grant from the Institute for Basic Science, Suwon, Republic of Korea (IBS-R015-D1). The work is supported by postdoctoral fellowships from BrainsCAN to Roy A. M. Haast and Yiming Xiao, and CIHR to Yiming Xiao. Support from CIHR Foundation grant FDN 201409 is also acknowledged. We would like to thank Catherine Currie for her assistance with recruiting participants for this study.

DATA AVAILABILITY STATEMENT

The template data have been deposited on the Open Science Framework website (<https://osf.io/c8p5n/>). Code to reproduce this analysis is available at <https://github.com/jclauneuro/zona-analysis/>. Videos in the study template space are provided with the main labels in each of the standard orientations as Supporting Information S6.

ORCID

- Jonathan C. Lau  <https://orcid.org/0000-0002-8452-8915>
- Yiming Xiao  <https://orcid.org/0000-0002-0962-3525>
- Roy A. M. Haast  <https://orcid.org/0000-0001-8543-2467>
- Greydon Gilmore  <https://orcid.org/0000-0001-7523-5734>
- Kâmil Uludag  <https://orcid.org/0000-0002-2813-5930>
- Ravi S. Menon  <https://orcid.org/0000-0002-7916-0263>
- Terry M. Peters  <https://orcid.org/0000-0003-1440-7488>
- Ali R. Khan  <https://orcid.org/0000-0002-0760-8647>

REFERENCES

- Akram, H., Dayal, V., Mahlknecht, P., Georgiev, D., Hyam, J., Foltyne, T., ... Zrinzo, L. (2018). Connectivity derived thalamic segmentation in deep brain stimulation for tremor. *NeuroImage: Clinical*, 18, 130–142. <https://doi.org/10.1016/j.nicl.2018.01.008>
- Al-Fatly, B., Ewert, S., Kübler, D., Kroneberg, D., Horn, A., & Kühn, A. A. (2019). Connectivity profile of thalamic deep brain stimulation to effectively treat essential tremor. *Brain* VIII–VIII, 142, 3086–3098. <https://doi.org/10.1093/brain/awz236>
- Amunts, K., Lepage, C., Borgeat, L., Mohlberg, H., Dickscheid, T., Rousseau, M.-É., ... Evans, A. C. (2013). BigBrain: An ultrahigh-resolution 3D human brain model. *Science*, 340, 1472–1475. <https://doi.org/10.1126/science.1235381>
- Avants, B. B., Tustison, N. J., Song, G., Cook, P. A., Klein, A., & Gee, J. C. (2011). A reproducible evaluation of ANTs similarity metric performance in brain image registration. *NeuroImage*, 54, 2033–2044. <https://doi.org/10.1016/j.neuroimage.2010.09.025>
- Bertrand, C., Hardy, J., Molina-Negro, P., & Martínez, N. (1969). Optimum physiological target for the arrest of tremor third symposium on Parkinson's disease (pp. 251–259). Edinburgh: Livingstone.
- Blomstedt, P., Sandvik, U., & Tisch, S. (2010). Deep brain stimulation in the posterior subthalamic area in the treatment of essential tremor. *Movement Disorders*, 25, 1350–1356. <https://doi.org/10.1002/mds.22758>
- Blomstedt, P., Stenmark Persson, R., Hariz, G.-M., Linder, J., Fredricks, A., Häggström, B., ... Hariz, M. (2018). Deep brain stimulation in the caudal zona incerta versus best medical treatment in patients with Parkinson's disease: a randomised blinded evaluation. *Journal of Neurology, Neurosurgery, and Psychiatry*, 89(7), 710–716. <https://doi.org/10.1136/jnnp-2017-317219>
- Castro, G., Carrillo-Ruiz, J. D., Salcido, V., Soto, J., García-Gomar, G., Velasco, A. L., & Velasco, F. (2015). Optimizing prelemniscal radiations as a target for motor symptoms in Parkinson's disease treatment. *Stereotactic and Functional Neurosurgery*, 93, 282–291. <https://doi.org/10.1159/000433446>
- Dallapiazza, R. F., Lee, D. J., De Vloo, P., Fomenko, A., Hamani, C., Hodaie, M., ... Lozano, A. M. (2018). Outcomes from stereotactic surgery for essential tremor. *Journal of Neurology, Neurosurgery, and Psychiatry*, 90(4), 474–482. <https://doi.org/10.1136/jnnp-2018-318240>
- DeKraker, J., Ferko, K. M., Lau, J. C., Köhler, S., & Khan, A. R. (2018). Unfolding the hippocampus: An intrinsic coordinate system for sub-field segmentations and quantitative mapping. *NeuroImage*, 167, 408–418. <https://doi.org/10.1016/j.neuroimage.2017.11.054>
- Dembek TA, Petry-schmelzer JN, Reker P, Hamacher S, Steffen J, Dafasari HS. 2019. PSA and VIM DBS efficiency in essential tremor depends on distance to the dentatorubrothalamic tract. *medRxiv*. <https://doi.org/10.1101/19013656>
- Deoni, S. C. L., Peters, T. M., & Rutt, B. K. (2005). High-resolution T1 and T2 mapping of the brain in a clinically acceptable time with DESPOT1 and DESPOT2. *Magnetic Resonance in Medicine*, 53, 237–241. <https://doi.org/10.1002/mrm.20314>
- Drain, L. E. (1949). A direct method of measuring nuclear spin-lattice relaxation times. *Proceedings of the Physical Society Section A*, 62, 301–306. <https://doi.org/10.1088/0370-1298/62/5/306>
- Eggenchwiler, F., Kober, T., Magill, A. W., Gruetter, R., & Marques, J. P. (2012). SA2RAGE: A new sequence for fast B1 + -mapping. *Magnetic Resonance in Medicine*, 67, 1609–1619. <https://doi.org/10.1002/mrm.23145>
- Fedorov, A., Beichel, R., Kalpathy-Cramer, J., Finet, J., Fillion-Robin, J. C., Pujol, S., ... Kikinis, R. (2012). 3D slicer as an image computing platform for the quantitative imaging network. *Magnetic Resonance Imaging*, 30, 1323–1341. <https://doi.org/10.1016/j.mri.2012.05.001>
- Fenoy, A. J., & Schiess, M. C. (2017). Deep brain stimulation of the Dentato-Rubro-thalamic tract: Outcomes of direct targeting for tremor. *Neuromodulation*, 20, 429–436. <https://doi.org/10.1111/ner.12585>
- Fiechter, M., Nowacki, A., Oertel, M. F., Fichtner, J., Deboe, I., Lachenmayer, M. L., ... Pollo, C. (2017). Deep brain stimulation for tremor: Is there a common structure? *Stereotactic and Functional Neurosurgery*, 95, 243–250. <https://doi.org/10.1159/000478270>

- Fonov, V., Evans, A., McKinstry, R., Almlí, C., & Collins, D. (2009). Unbiased nonlinear average age-appropriate brain templates from birth to adulthood. *NeuroImage*, 47, S102–S102. [https://doi.org/10.1016/S1053-8119\(09\)70884-5](https://doi.org/10.1016/S1053-8119(09)70884-5)
- Forel, A. (1877). Untersuchungen über die Haubenregion und ihre oberen Verknüpfungen im Gehirne des Menschen und einiger Säugetiere, mit Beiträgen zu den Methoden der Gehirnuntersuchung. *Archiv für Psychiatrie Und Nervenkrankheiten*, 7, 393–495. <https://doi.org/10.1007/BF02041873>
- Forstmann, B. U., Keuken, M. C., Schafer, A., Bazin, P., Alkemade, A., & Turner, R. (2014). Multi-modal ultra-high resolution structural 7-Tesla MRI data repository. *Scientific Data*, 1, 140050. <https://doi.org/10.1038/sdata.2014.50>
- Gallay, M. N., Jeanmonod, D., Liu, J., & Morel, A. (2008). Human pallidothalamic and cerebellothalamic tracts: Anatomical basis for functional stereotactic neurosurgery. *Brain Structure & Function*, 212, 443–463. <https://doi.org/10.1007/s00429-007-0170-0>
- Gilbert, K. M., Curtis, A. T., Gati, J. S., Klassen, L. M., & Menon, R. S. (2011). A radiofrequency coil to facilitate B 1 + shimming and parallel imaging acceleration in three dimensions at 7 T. *NMR in Biomedicine*, 24, 815–823. <https://doi.org/10.1002/nbm.1627>
- Glasser, M. F., Sotiropoulos, S. N., Wilson, J. A., Coalson, T. S., Fischl, B., Andersson, J. L., ... Jenkinson, M. (2013). The minimal preprocessing pipelines for the human connectome project. *NeuroImage*, 80, 105–124. <https://doi.org/10.1016/j.neuroimage.2013.04.127>
- Gorgolewski, K. J., Alfaro-almagro, F., Auer, T., Bellec, P., Capotă, M., Chakravarty, M. M., ... Yarkoni, T. (2017). BIDS apps: Improving ease of use, accessibility, and reproducibility of neuroimaging data analysis methods. *PLoS Computational Biology*, 13, e1005209. <https://doi.org/10.1371/journal.pcbi.1005209>
- Gorgolewski KJ, Auer T, Calhoun VD, Craddock RC, Das S. 2016. The brain imaging data structure, a format for organizing and describing outputs of neuroimaging experiments 3:1–9.
- Haacke, E. M., Cheng, N. Y. C., House, M. J., Liu, Q., Neelavalli, J., Ogg, R. J., ... Obenaus, A. (2005). Imaging iron stores in the brain using magnetic resonance imaging. *Magnetic Resonance Imaging*, 23, 1–25. <https://doi.org/10.1016/j.mri.2004.10.001>
- Haast, R. A., Lau, J. C., Ivanov, D., Menon, R. S., Uludağ, K., & Khan, A. R. (2020). Effects of MP2RAGE B1+ sensitivity on inter-site T1 reproducibility and morphometry at 7T. *bioRxiv*, 2, 1–2. <https://doi.org/10.1101/2020.02.13.947382>
- Hahn, E. L. (1949). An accurate nuclear magnetic resonance method for measuring spin-lattice relaxation times. *Physics Review*, 76, 145–146. <https://doi.org/10.1103/PhysRev.76.145>
- Hariz, M., & Blomstedt, P. (2017). Surgical management of tremor. *Youngs neurological surgery*, 6, (pp. 602–609). Philadelphia, PA: Elsevier Inc.
- Hawrylycz, M. J., Lein, E. S., Guillozet-Bongaarts, A. L., Shen, E. H., Ng, L., Miller, J. A., ... Jones, A. R. (2012). An anatomically comprehensive atlas of the adult human brain transcriptome. *Nature*, 489, 391–399. <https://doi.org/10.1038/nature11405>
- Herrington, T. M., Cheng, J. J., & Eskandar, E. N. (2016). Mechanisms of deep brain stimulation. *Journal of Neurophysiology*, 115, 19–38. <https://doi.org/10.1152/jn.00281.2015>
- Horn, A., Reich, M., Vorwerk, J., Li, N., Wenzel, G., Fang, Q., ... Fox, M. D. (2017). Connectivity predicts deep brain stimulation outcome in Parkinson disease. *Annals of Neurology*, 82, 67–78. <https://doi.org/10.1002/ana.24974>
- Kerl, H. U., Gerigk, L., Brockmann, M. A., Huck, S., Al-Zghloul, M., Groden, C., ... Nölte, I. S. (2013). Imaging for deep brain stimulation: The zona incerta at 7 Tesla. *World Journal of Radiology*, 5, 5–16. <https://doi.org/10.4329/wjr.v5.i1.5>
- Keuken, M. C., Bazin, P.-L., Backhouse, K., Beekhuizen, S., Himmer, L., Kandola, A., ... Forstmann, B. U. (2017). Effects of aging on T1, T2, and QSM MRI values in the subcortex. *Brain Structure & Function*, 58, 7250–7257. <https://doi.org/10.1007/s00429-016-1352-4>
- Keuken, M. C., Bazin, P.-L., Schafer, A., Neumann, J., Turner, R., & Forstmann, B. U. (2013). Ultra-high 7T MRI of structural age-related changes of the subthalamic nucleus. *The Journal of Neuroscience*, 33, 4896–4900. <https://doi.org/10.1523/JNEUROSCI.3241-12.2013>
- Lau, J. C., Khan, A. R., Zeng, T. Y., MacDougall, K. W., Parrent, A. G., & Peters, T. M. (2018). Quantification of local geometric distortion in structural magnetic resonance images: Application to ultra-high fields. *NeuroImage*, 168, 141–151. <https://doi.org/10.1016/j.neuroimage.2016.12.066>
- Lau, J. C., Parrent, A. G., Demarco, J., Gupta, G., Kai, J., Stanley, O. W., ... Peters, T. M. (2019). A framework for evaluating correspondence between brain images using anatomical fiducials. *Human Brain Mapping*, 40, 4163–4179. <https://doi.org/10.1002/hbm.24693>
- Li, X., Morgan, P. S., Ashburner, J., Smith, J., & Rorden, C. (2016). The first step for neuroimaging data analysis: DICOM to NIfTI conversion. *Journal of Neuroscience Methods*, 264, 47–56. <https://doi.org/10.1016/j.jneumeth.2016.03.001>
- Llinás, R., & Jahnsen, H. (1982). Electrophysiology of mammalian thalamic neurones in vitro. *Nature*, 297, 406–408. <https://doi.org/10.1038/297406a0>
- Luigi, Z., Youdim, M. B. H., Riederer, P., Connor, J. R., & Crichton, R. R. (2004). Iron, brain ageing and neurodegenerative disorders. *Nature Reviews Neuroscience*, 5, 863–873. <https://doi.org/10.1038/nrn1537>
- Ma, T. P., Johnson, J. C., & Hoskins, G. A. (1997). Organization of the zona incerta in the macaque: An electron microscopic study. *The Anatomical Record*, 229, 259–275. [https://doi.org/10.1002/\(SICI\)1097-0185\(199710\)249:2<259::AID-AR14>3.0.CO;2-N](https://doi.org/10.1002/(SICI)1097-0185(199710)249:2<259::AID-AR14>3.0.CO;2-N)
- Mai, J., Majtanik, M., & Paxinos, G. (2015). *Atlas of the human brain* (4th ed.). London, England: Elsevier.
- Maier-Hein, K. H., Neher, P. F., Houde, J.-C., Côté, M.-A., Garyfallidis, E., Zhong, J., ... Descoteaux, M. (2017). The challenge of mapping the human connectome based on diffusion tractography. *Nature Communications*, 8, 1349. <https://doi.org/10.1038/s41467-017-01285-x>
- Manjón, J. V., Coupé, P., Martí-Bonmatí, L., Collins, D. L., & Robles, M. (2010). Adaptive nonlocal means denoising of MR images with spatially varying noise levels. *Journal of Magnetic Resonance Imaging*, 31, 192–203. <https://doi.org/10.1002/jmri.22003>
- Marques, J. P., & Gruetter, R. (2013). New developments and applications of the MP2RAGE sequence - Focusing the contrast and high spatial resolution R1 mapping. *PLoS One*, 8, e69294. <https://doi.org/10.1371/journal.pone.0069294>
- Marques, J. P., Kober, T., Krueger, G., van der Zwaag, W., Van de Moortele, P.-F., & Gruetter, R. (2010). MP2RAGE, a self bias-field corrected sequence for improved segmentation and T1-mapping at high field. *NeuroImage*, 49, 1271–1281. <https://doi.org/10.1016/j.neuroimage.2009.10.002>
- Marques, J. P., & Norris, D. G. (2017). How to choose the right MR sequence for your research question at 7 T and above? *NeuroImage*, 168, 119–140. <https://doi.org/10.1016/j.neuroimage.2017.04.044>
- Masri, R., Quiton, R. L., Lucas, J. M., Murray, P. D., Thompson, S. M., & Keller, A. (2009). Zona Incerta: A Role in Central Pain. *Journal of Neurophysiology*, 102, 181–191. <https://doi.org/10.1152/jn.00152.2009>
- Mitrofanis, J. (2005). Some certainty for the "zone of uncertainty"? Exploring the function of the zona incerta. *Neuroscience*, 130, 1–15. <https://doi.org/10.1016/j.neuroscience.2004.08.017>
- Mohadjer, M., Goerke, H., Milius, E., Etou, A., & Mundinger, F. (1990). Long-term results of stereotaxy in the treatment of essential tremor. *Stereotactic and Functional Neurosurgery*, 54–55, 125–129. <https://doi.org/10.1159/000100201>
- Morel, A. (2007). *Stereotactic atlas of the human thalamus and basal ganglia*. New York: Informa Healthcare.

- Morel, A., Magnin, M., & Jeanmonod, D. (1997). Multiarchitectonic and stereotactic atlas of the human thalamus. *The Journal of Comparative Neurology*, 387, 588–630.
- Mundinger, F. (1965). Stereotaxic interventions on the zona incerta area for treatment of extrapyramidal motor disturbances and their results. *Stereotactic and Functional Neurosurgery*, 26, 222–230. <https://doi.org/10.1159/000104030>
- Nieuwenhuys, R., Voogd, J., & van Huijzen, C. (2007). *The human central nervous system* (4th ed.). Berlin, Germany: Springer-Verlag.
- Nowacki, A., Debove, I., Rossi, F., Schlaeppe, J. A., Petermann, K., Wiest, R., ... Pollo, C. (2018). Targeting the posterior subthalamic area for essential tremor: Proposal for MRI-based anatomical landmarks. *Journal of Neurosurgery*, 131, 1–8. <https://doi.org/10.3171/2018.4.JNS18373>
- Nowacki, A., Nguyen, T. A. K., Tinkhauser, G., Petermann, K., Debove, I., Wiest, R., & Pollo, C. (2018). Accuracy of different three-dimensional subcortical human brain atlases for DBS –lead localisation. *NeuroImage Clin*, 20, 868–874. <https://doi.org/10.1016/j.nicl.2018.09.030>
- Plaha, P., Ben-Shlomo, Y., Patel, N. K., & Gill, S. S. (2006). Stimulation of the caudal zona incerta is superior to stimulation of the subthalamic nucleus in improving contralateral parkinsonism. *Brain*, 129, 1732–1747. <https://doi.org/10.1093/brain/awl127>
- Plantinga, B. R., Temel, Y., Duchin, Y., Uludağ, K., Patriat, R., Roebroek, A., ... Harel, N. (2018). Individualized parcellation of the subthalamic nucleus in patients with Parkinson's disease with 7T MRI. *NeuroImage*, 168, 403–411. <https://doi.org/10.1016/j.neuroimage.2016.09.023>
- Power, B. D., & Mitrofanis, J. (2001). Zona incerta: Substrate for contralateral interconnectivity in the thalamus of rats. *The Journal of Comparative Neurology*, 436, 52–63. <https://doi.org/10.1002/cne.1053>
- Puelles, L., Martinez-de-la-Torre, M., Ferran, J.-L., & Watson, C. (2012). Diencephalon. In *The mouse nervous system* (pp. 313–336). London, England: Elsevier. <https://doi.org/10.1016/B978-0-12-369497-3.10009-3>
- Rioux, J. A., Levesque, I. R., & Rutt, B. K. (2016). Biexponential longitudinal relaxation in white matter: Characterization and impact on T1mapping with IR-FSE and MP2RAGE. *Magnetic Resonance in Medicine*, 75, 2265–2277. <https://doi.org/10.1002/mrm.25729>
- Rooney, W. D., Johnson, G., Li, X., Cohen, E. R., Kim, S. G., Ugurbil, K., & Springer, C. S. (2007). Magnetic field and tissue dependencies of human brain longitudinal $^1\text{H}_2\text{O}$ relaxation in vivo. *Magnetic Resonance in Medicine*, 57, 308–318. <https://doi.org/10.1002/mrm.21122>
- Rudko, D. A., Klassen, L. M., de Chickera, S. N., Gati, J. S., Dekaban, G. A., & Menon, R. S. (2014). Origins of $\text{R}2^*$ orientation dependence in gray and white matter. *Proceedings of the National Academy of Sciences of the United States of America*, 111, E159–E167. <https://doi.org/10.1073/pnas.1306516111>
- Sammartino, F., Krishna, V., King, N. K. K., Lozano, A. M., Schwartz, M. L., Huang, Y., & Hodaie, M. (2016). Tractography-based ventral intermediate nucleus targeting: Novel methodology and intraoperative validation. *Movement Disorders*, 31, 1217–1225. <https://doi.org/10.1002/mds.26633>
- Schäfer, A., Forstmann, B. U., Neumann, J., Wharton, S., Mietke, A., Bowtell, R., & Turner, R. (2012). Direct visualization of the subthalamic nucleus and its iron distribution using high-resolution susceptibility mapping. *Human Brain Mapping*, 33, 2831–2842. <https://doi.org/10.1002/hbm.21404>
- Schaltenbrand, G., & Wahren, W. (1977). *Atlas for stereotaxy of the human brain* (2nd ed.). Stuttgart, Germany: Thieme.
- Sled, J. G., Zijdenbos, A. P., & Evans, A. C. (1998). A nonparametric method for automatic correction of intensity nonuniformity in MRI data. *IEEE Transactions on Medical Imaging*, 17, 87–97. <https://doi.org/10.1109/42.668698>
- Spiegel, E., Wycis, H., Szekely, E., Baird, H., Adams, J., III, & Flanagan, M. (1962). Campotomy. *Transactions of the American Neurological Association*, 87, 240–242.
- Spiegel, E. A., & Wycis, H. T. (1954). Anotomy in Paralysis Agitans. *Archives of Neurology and Psychiatry*, 71, 598–614. <https://doi.org/10.1001/archneurpsyc.1954.02320410060005>
- Spiegel, E. A., Wycis, H. T., Szekely, E. G., Soloff, L., Adams, J., Gildenberg, P., & Zanes, C. (1964). Stimulation of Forel's field during stereotaxic operations in the human brain. *Electroencephalography and Clinical Neurophysiology*, 16, 537–548. [https://doi.org/10.1016/0013-4694\(64\)90045-8](https://doi.org/10.1016/0013-4694(64)90045-8)
- Stikov, N., Boudreau, M., Levesque, I. R., Tardif, C. L., Barral, J. K., & Pike, G. B. (2015). On the accuracy of T1 mapping: Searching for common ground. *Magnetic Resonance in Medicine*, 73, 514–522. <https://doi.org/10.1002/mrm.25135>
- Teeuwisse, W. M., Brink, W. M., Haines, K. N., & Webb, A. G. (2012). Simulations of high permittivity materials for 7 T neuroimaging and evaluation of a new barium titanate-based dielectric. *Magnetic Resonance in Medicine*, 67, 912–918. <https://doi.org/10.1002/mrm.24176>
- Tourdias, T., Saranathan, M., Levesque, I. R., Su, J., & Rutt, B. K. (2014). Visualization of intra-thalamic nuclei with optimized white-matter-nulled MPRAGE at 7T. *NeuroImage*, 84, 534–545. <https://doi.org/10.1016/j.neuroimage.2013.08.069>
- Trampel, R., Bazin, P.-L., Pine, K., & Weiskopf, N. (2017). In-vivo magnetic resonance imaging (MRI) of laminae in the human cortex. *NeuroImage*, 197, 1–9. <https://doi.org/10.1016/j.neuroimage.2017.09.037>
- Truini, A., Garcia-Larrea, L., & Crucu, G. (2013). Reappraising neuropathic pain in humans—How symptoms help disclose mechanisms. *Nature Reviews Neurology*, 9, 572–582. <https://doi.org/10.1038/nrneurol.2013.180>
- Tustison, N. J., Avants, B. B., Cook, P. A., Zheng, Y., Egan, A., Yushkevich, P. A., & Gee, J. C. (2010). N4ITK: Improved N3 bias correction. *IEEE Transactions on Medical Imaging*, 29, 1310–1320.
- Velasco, F., Esqueda-Liquidano, M., Velasco, A. L., & García-Gomar, M. G. (2018). Prelemniscal lesion for selective improvement of Parkinson disease tremor. *Stereotactic and Functional Neurosurgery*, 96, 54–59. <https://doi.org/10.1159/000486318>
- Velasco, F., Jiménez, F., Pérez, M. L., Carrillo-Ruiz, J. D., Velasco, A. L., Ceballos, J., & Velasco, M. (2001). Electrical stimulation of the prelemniscal radiation in the treatment of Parkinson's disease: An old target revised with new techniques. *Neurosurgery*, 49, 293–308. <https://doi.org/10.1097/00006123-200108000-00009>
- Velasco, F., Velasco, M., & Machado, J. P. (1975). A statistical outline of the subthalamic target for the arrest of tremor. *Stereotactic and Functional Neurosurgery*, 38, 38–46. <https://doi.org/10.1159/000102641>
- Velasco, F. C., Molina-Negro, P., Bertrand, C., & Hardy, J. (1972). Further definition of the subthalamic target for arrest of tremor. *Journal of Neurosurgery*, 36, 184–191. <https://doi.org/10.3171/jns.1972.36.2.0184>
- Venkataraman, A., Brody, N., Reddi, P., Guo, J., Gordon Rainnie, D., & Dias, B. G. (2019). Modulation of fear generalization by the zona incerta. *Proceedings of the National Academy of Sciences*, 116, 9072–9077. <https://doi.org/10.1073/pnas.1820541116>
- Watson, C., Lind, C. R. P., & Thomas, M. G. (2014). The anatomy of the caudal zona incerta in rodents and primates. *Journal of Anatomy*, 224, 95–107. <https://doi.org/10.1111/joa.12132>
- Wertheimer, P., Lapras, C., & Levy, A. (1960). *Essais de chirurgie thalamique [Trials in thalamic surgery]*. Neurochirurgie, 6, 105–112.
- Xiao, Y., Fonov, V., Bériault, S., Al, S. F., Chakravarty, M. M., Sadikot, A. F., ... Collins, D. L. (2014). Multi-contrast unbiased MRI atlas of a Parkinson's disease population. *International Journal of Computer Assisted Radiology and Surgery*, 10, 329–341. <https://doi.org/10.1007/s11548-014-1068-y>
- Xiao, Y., Jannin, P., D'Albis, T., Guizard, N., Haegelen, C., Lalys, F., ... Collins, D. L. (2014). Investigation of morphometric variability of subthalamic nucleus, red nucleus, and substantia nigra in advanced Parkinson's disease patients using automatic segmentation and PCA-based analysis. *Human Brain Mapping*, 35, 4330–4344. <https://doi.org/10.1002/hbm.22478>
- Xiao, Y., Lau, J. C., Anderson, T., DeKraker, J., Collins, D. L., Peters, T., & Khan, A. R. (2019). An accurate registration of the BigBrain dataset

- with the MNI PD25 and ICBM152 atlases. *Scientific Data*, 6, 210. <https://doi.org/10.1038/s41597-019-0217-0>
- Zecca, L., Stroppolo, A., Gatti, A., Tampellini, D., Toscani, M., Gallorini, M., ... Zucca, F. A. (2004). The role of iron and copper molecules in the neuronal vulnerability of locus coeruleus and substantia nigra during aging. *Proceedings of the National Academy of Sciences*, 101, 9843–9848. <https://doi.org/10.1073/pnas.0403495101>
- Zhao, Z., Zongming, C., Xiang, X., Hu, M., Xie, H., Jia, X., ... Shen, W. L. (2019). Zona incerta GABAergic neurons integrate prey-related sensory signals and induce an appetitive drive to promote hunting. *Nature Neuroscience*, 22, 921–932. <https://doi.org/10.1038/s41593-019-0404-5>

SUPPORTING INFORMATION

Additional supporting information may be found online in the Supporting Information section at the end of this article.

How to cite this article: Lau JC, Xiao Y, Haast RAM, et al.

Direct visualization and characterization of the human zona incerta and surrounding structures. *Hum Brain Mapp*. 2020; 1–18. <https://doi.org/10.1002/hbm.25137>